Astronomy & Astrophysics manuscript no. output
April 19, 2026

First detection of X-ray polarization from the long-period X-ray pulsar 4U 1954+319

Alexander Salganik[1], Lingda Kong[2], Sofia V. Forsblom[1], Menglei Zhou[2], Honghui Liu[2], QingChang Zhao[3,4], Sergey S. Tsygankov[1,2,3], Andrea Santangelo[2], Juri Poutanen[1]

[1] Department of Physics and Astronomy, 20014 University of Turku, Finland
e-mail: alsalganik@gmail.com
[2] Institut für Astronomie und Astrophysik, Universität Tübingen, Sand 1, 72076 Tübingen, Germany
[3] Key Laboratory of Particle Astrophysics, Institute of High Energy Physics, Chinese Academy of Sciences, Beijing 100049, China
[4] University of Chinese Academy of Sciences, Chinese Academy of Sciences, Beijing 100049, China

Received XXX

ABSTRACT

We report the first detection of X-ray polarization with the *Imaging X-ray Polarimetry Explorer* from the X-ray pulsar (XRP) 4U 1954+319. The source belongs to an extremely rare class of systems in which a slowly rotating neutron star accretes from the dense wind of a red supergiant companion. We detect coherent pulsations at $P_{\rm spin} = 5.49 \pm 0.05$ h, which is one of the longest spin periods known among XRPs. While the phase-averaged analysis shows no significant polarization, with a 99% confidence minimum detectable polarization ($\rm MDP_{99}$) of 4.9% in the 2–8 keV band, the phase-resolved analysis shows a single interval at pulse maximum in which the polarization degree (PD) exceeds the $\rm MDP_{99}$, yielding PD $= 10.2^{+3.1}_{-3.0}$%. The polarization angle (PA) exhibits a smooth $\approx 150^\circ$ rotation over the pulse, and a joint evaluation of all phase bins yields an overall detection significance of 3.3σ. Using the rotating vector model, we identify a geometric solution that reproduces the observed PA variation. From this model, we infer a phase-independent PD of 6.1 ± 1.1% in the 2–8 keV band.

Key words. accretion, accretion disks – magnetic fields – pulsars: individual: 4U 1954+319 – stars: neutron – X-rays: binaries

1. Introduction

Neutron stars (NSs) are among the most extreme objects in the Universe, with surface magnetic fields spanning $\sim 10^8$ G in recycled millisecond pulsars, $\sim 10^{11}$–10^{13} G in ordinary pulsars, and up to $\sim 10^{14}$–10^{15} G in magnetars. In accreting binary systems, they manifest as X-ray pulsars (XRPs), which serve as natural laboratories for studying accretion physics, magnetospheric interactions, and quantum electrodynamic effects in strong fields (Mushtukov & Tsygankov 2024). Their X-ray emission is fueled by the accretion of matter from the companion star, producing hot spots or accretion columns near the NS magnetic poles. The structure and geometry of this emission region are primarily governed by the magnetic field strength and the accretion rate. XRPs occur in both low-mass X-ray binaries (LMXBs; Avakyan et al. 2023) and high-mass X-ray binaries (HMXBs; Neumann et al. 2023).

Among X-ray binaries, 4U 1954+319 represents a particularly unusual case. The donor star was originally classified as an M4–5 III giant (Masetti et al. 2006), which led to its identification as a symbiotic X-ray binary (SyXRB), a subclass of LMXBs where an NS accretes from the dense wind of an evolved late-type giant (see Bahramian & Degenaar 2024, for a review). However, later observations revealed that the donor is a red supergiant (RSG) of spectral type M4 I (Hinkle et al. 2020), implying that 4U 1954+319 is an HMXB rather than a SyXRB. While most known HMXBs host blue supergiant or Be-type donors, 4U 1954+319 stands out as one of only two confirmed Galactic systems containing an NS accreting from an RSG, the other being SWIFT J0850.8−4219 (De et al. 2024). The updated classification and revised stellar parameters indicate a donor mass of $\sim 9\,M_\odot$, a radius of $\sim 590\,R_\odot$ (Hinkle et al. 2020), and a *Gaia* DR3 distance of $d = 3.89^{+0.33}_{-0.28}$ kpc (Wang & Li 2025, their Table 2). These properties imply a binary separation of at least 5 au and an orbital period longer than three years (Hinkle et al. 2020).

Corbet et al. (2006, 2008) discovered pulsations from 4U 1954+319 with a period of about 5 h, establishing it as one of the slowest known XRPs. The NS spin period exhibits substantial long-term variations of more than 10% with alternating spin-up and spin-down episodes (Marcu et al. 2011; Enoto et al. 2014). The pulse profile in the 2–8 keV range of the *Imaging X-ray Polarimetry Explorer* (*IXPE*) shows a complex morphology characterized by two broader maxima and multiple subpeaks with a pulsed fraction (PF) of approximately 60–80% (Enoto et al. 2014). Bozzo et al. (2022) used hardness-ratio resolved spectroscopy with *X-ray Multi-Mirror Mission (XMM-Newton)* and *Nuclear Spectroscopic Telescope Array (NuSTAR)* observatories to reveal variability consistent with accretion from a clumpy RSG wind.

The nature of 4U 1954+319 makes it not only an evolutionary outlier among X-ray binaries, but also a key test case for accretion theory. The low bolometric luminosity (up to $\sim 10^{36}$ erg s^{-1}; Marcu et al. 2011; Enoto et al. 2014; Bozzo et al. 2022), the extremely long spin period, and the wind-fed accretion scenario are difficult to reconcile with standard angular momentum transfer models such as the magnetically threaded accretion disk model of Ghosh & Lamb (1979, see, e.g., Mao & Li 2024). In contrast, the subsonic settling accretion model (Shakura et al. 2012), especially when modified

Article published by EDP Sciences, to be cited as https://doi.org/10.1051/0004-6361/202558439

to include stochastic reversals of the accreted angular momentum (Mao & Li 2024), explains the observed properties without requiring previously suggested magnetar-strength fields (Bozzo et al. 2022).

Although spectral and timing analyses have constrained the accretion regime of 4U 1954+319, they cannot reveal the orientation of the magnetic field or the overall emission geometry. X-ray polarimetry with IXPE now makes this possible and provides direct insights into the system's accretion configuration.

In this work, we report the first detection of X-ray polarization in an XRP with an RSG companion, obtained for 4U 1954+319 with *IXPE*. We detected the polarization signal in the phase-resolved analysis, while the phase-averaged emission showed no significant polarization. Salganik et al. (2025) presents the preliminary results. The remainder of this paper is organized as follows. Section 2 provides an overview of the observational methods and data sets used. The main results are presented in Sect. 3. Finally, Sect. 4 presents the constraints on the pulsar geometry, and Sect. 5 summarizes our findings.

2. Observations and data reduction

2.1. IXPE

The *IXPE* observatory (Weisskopf et al. 2022) carries three identical detector units (DUs), each equipped with a gas pixel detector (Baldini et al. 2021; Soffitta et al. 2021). Observations with the *IXPE* covered 4U 1954+319 from 16 to 21 October 2025 (ObsID 04251201), for a total exposure of about 194 ks per DU. During this observation, data from DU2 were unavailable due to pixel failures that occurred in April 2025, so the analysis relied solely on photons detected by DU1 and DU3.

We extracted spectral and polarimetric products using the `ixpestartx`[1] task, which uses the standard HEASoft v6.36 together with the most recent *IXPE* calibration files (CALDB v.20250225). We adopted a circular extraction region of 80″ radius centered on the source (R.A. = $19^h55^m42^s$, Dec. = +32°05′49″). We tested weighted analysis and background subtraction using different annular regions centered on the source and found no significant improvement in the polarization constraints. We therefore adopted an unweighted analysis without background subtraction. In all event files, we rejected events with a nonzero status column, thereby removing events flagged as instrumental background or otherwise problematic.

We obtained the polarization degree (PD) and polarization angle (PA) parameters using two complementary approaches: (1) a model-independent analysis with the `ixpepolarization` tool in HEASoft (see also Kislat et al. 2015) and (2) spectro-polarimetric fitting with `xspec`. In addition to the phase-averaged analysis, we performed a phase-resolved study. We filtered barycenter-corrected (via `barycorr`) event lists in phase by assigning each photon to the appropriate phase bin. We did not apply a binary motion correction because the complete set of source orbital parameters remains unknown. For each phase bin, we generated spectra and responses with `ixpestartx` and then grouped them with `ftgrouppha`, requiring a minimum of 20 counts per bin and using the same energy bins for I, Q, and U. We fit the resulting spectra with XSPEC v. 12.15.1 (Arnaud 1996).

[1] `https://heasarc.gsfc.nasa.gov/docs/ixpe/analysis/contributed/ixpestartx.html`

2.2. NuSTAR

NuSTAR comprises two identical, co-aligned X-ray focal plane modules, FPMA and FPMB (Harrison et al. 2013), which provide sensitive coverage in the 3–79 keV energy band. Observations were performed on 2025 October 16 (ObsID 91102340002) and on 2025 October 18 (ObsID 91102340004), hereafter referred to as NuObs1 and NuObs2, respectively. We extracted the source events using a circular region with a 50″ radius centered on the source position. We chose a 120″ radius background region to optimize the signal-to-noise ratio, particularly at higher energies.

We reduced the *NuSTAR* observations following the standard processing guidelines.[2] The data were processed using HEASOFT v6.36 and CALDB version 20251006 (including the clock correction file 20100101v215). We produced cleaned event files with the task `nupipeline`. To mitigate background enhancements associated with passages through the South Atlantic Anomaly (SAA), we applied the filtering configuration recommended by the official SAA reports for these sequences, namely `saacalc=2`, `saamode=OPTIMIZED` and `tentacle=no`, which preserves essentially all useful exposure (21.3 and 19.4 ks for NuObs1 and NuObs2, respectively). We extracted the spectra with the `nuproducts` tool as part of the `nustardas` pipeline and grouped them to have at least 20 counts per energy channel. Significant stray-light contamination affected FPMB during NuObs1 and NuObs2; therefore, we excluded this module from the spectral analysis.

Throughout this paper we calculate all luminosities assuming the *Gaia* DR3 distance of $d = 3.89$ kpc (Wang & Li 2025). We adopt the abundances of Wilms et al. (2000) for the modeling of photoabsorption. We perform spectral fits using χ^2 statistics and quote uncertainties at the 68.3% confidence level (CL; 1σ), unless otherwise stated.

3. Results

3.1. Timing analysis

For the timing analysis, we extracted 2–8 keV light curves from the event files of DU1 and DU3. Using XSELECT, we applied an energy filter and selected source photons from the same circular region used for the spectral analysis. We produced light curves with a time bin of 1 s, and summed the resulting curves from DU1 and DU3 using the `lcmath` procedure. Figure 1 shows the resulting summed 2–8 keV light curve.

The χ^2 periodogram gives a peak at 5.49 ± 0.05 h (Fig. 2). We estimated the uncertainty using a bootstrap resampling procedure, randomizing the light curve repeatedly within its statistical uncertainties and fitting the main peak of the periodogram with a Gaussian. This period corresponds to the NS spin period of ~ 5 h (Corbet et al. 2006, 2008) and serves as the basis for the phase-resolved polarimetric analysis presented below.

Folding the 2–8 keV light curve on this period yields a complex pulse profile (Fig. 3a). The profile shows two maxima and multiple subpeaks. The light curve does not show statistically significant variability that would indicate changes in the spectral state during the *IXPE* observation. The pulse profile, overplotted on the light curve, follows the data without indicating long-term deviations indicative of additional variability (Fig. 1). This suggests that no strong changes in the dominant polarization properties occur over the course of the observation.

[2] `https://heasarc.gsfc.nasa.gov/docs/nustar/analysis/nustar_swguide.pdf`

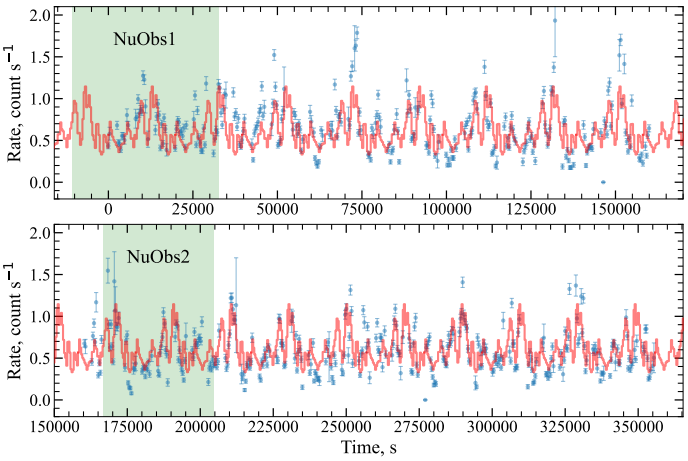

Fig. 1: Light curve of 4U 1954+319 in the 2–8 keV band during the *IXPE* observation, rebinned to 366 s. The zero time corresponds to the start of the *IXPE* observation. Shaded regions mark the time intervals of the two *NuSTAR* observations (NuObs1 and NuObs2). The solid curve shows the pulse profile repeated over the spin period.

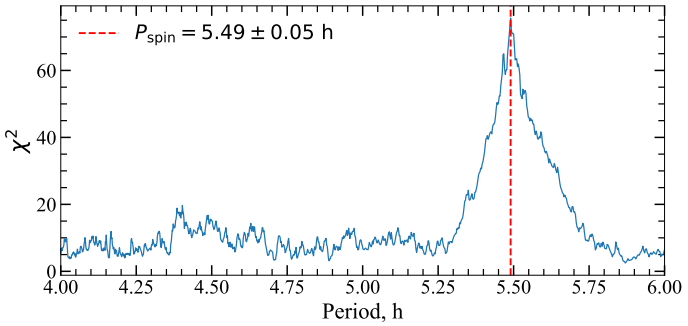

Fig. 2: χ^2 periodogram of the 2–8 keV *IXPE* light curve. The best-fit period is indicated by the vertical dashed line.

3.2. Phase-averaged polarimetric analysis

We performed two separate phase-averaged joint spectral and polarimetric fits in XSPEC. Each fit combined the full *IXPE* dataset with a different quasi-simultaneous *NuSTAR* observation, namely NuObs1 and NuObs2. In both cases, the *IXPE* data consisted of six spectra corresponding to Stokes I, Q, and U from DU1 and DU3. We initially adopted the model `const×tbabs×[cutoffpl×polconst+gaussian]`, where `const` accounts for cross-calibration offsets between instruments (with DU1 fixed to unity), `tbabs` models interstellar absorption, `polconst` assumes energy-independent polarization across the *IXPE* band, and the Gaussian component represents the Fe Kα emission around 6.4 keV.

When fitting NuObs1+*IXPE*, the baseline model does not fully describe the data (χ^2/d.o.f. = 1.09), leaving systematic residuals in the form of a broad hump at 20–30 keV. To account for this feature, we included an additional `bbodyrad` component, resulting in the final model `const×tbabs×[(cutoffpl+bbodyrad)×polconst + gaussian]`. The additional component has a temperature of $kT \approx 1.5$ keV and an emitting radius of $\sim$ 600 m, improving the fit to χ^2/d.o.f. = 1.06 and substantially reducing the residual structure. The same extended model yields an acceptable fit for NuObs2+*IXPE* (χ^2/d.o.f. = 0.92), with no notable residuals in either dataset, including the energy range around the iron line.

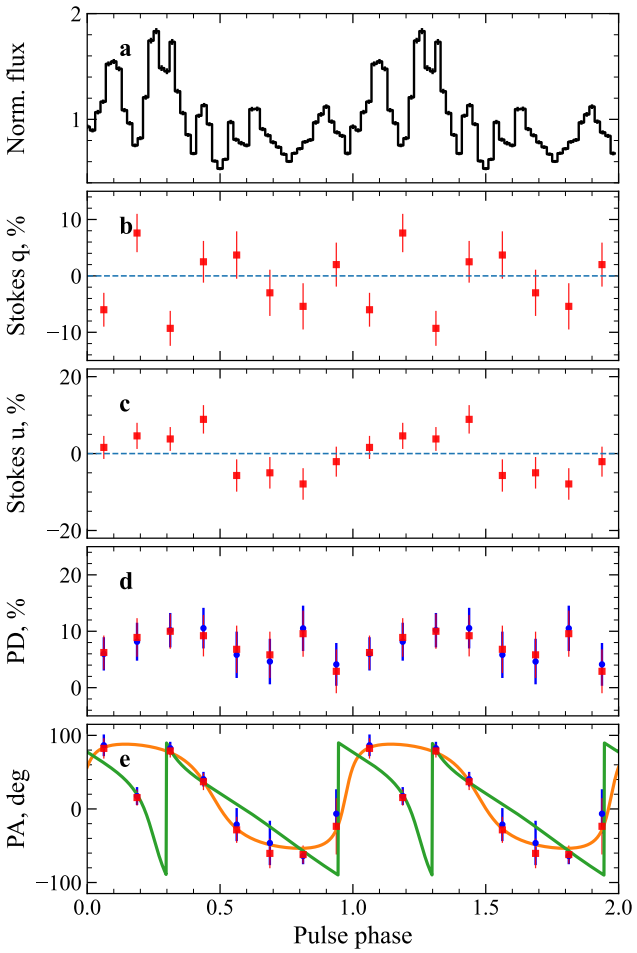

Fig. 3: Phase-resolved properties of 4U 1954+319 over two pulse cycles. The PD and PA measurements derive from two methods: blue points show spectro-polarimetric analysis results, and square red symbols show model-independent measurements obtained with `ixpepolarization`. Panels display (a) the normalized pulse profile in the 2–8 keV band derived from the IXPE data, (b)–(c) the Stokes parameters q and u, (d) the PD, and (e) the PA. The PA panel shows two RVM solutions from Table 3, corresponding to two distinct posterior clusters in Fig. 6: Solution 1 (orange) and Solution 2 (green).

The joint NuObs2+*IXPE* fit also shows better overall consistency between the two observatories than the NuObs1+*IXPE* case. We therefore adopted the NuObs2-based parameters as our final phase-averaged spectral–polarimetric results. Our analysis does not significantly detect phase-averaged polarization and constrains it with an upper limit of 5.1% (corresponding to MDP$_{99}$). Table 1 (see also Fig. 4) lists the best-fitting spectral and polarimetric parameters.

We further investigated the energy dependence of the polarization in 4U 1954+319 by dividing the 2–8 keV band into three sub-bands: 2–4, 4–6, and 6–8 keV. We performed energy-resolved spectro-polarimetric fits for each energy interval using the same model configuration, with the Stokes Q and U spectra restricted to the corresponding energy bins. We could not significantly constrain the PD in any of these bands and therefore report MDP$_{99}$ upper limits of 5.2%, 5.2%, and 6.1% for the 2–4, 4–6, and 6–8 keV bands, respectively.

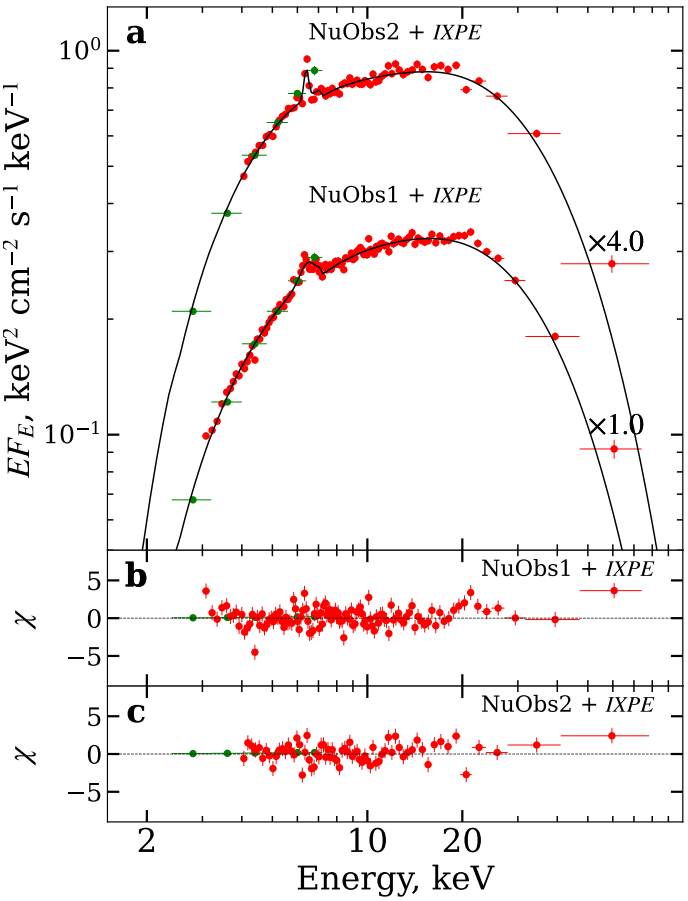

Fig. 4: Unfolded energy spectra from the joint *IXPE* and *NuSTAR* analysis. The *IXPE* spectra correspond to the Stokes *I* datasets from DU1 and DU3. Green points denote the *IXPE* measurements, while red points represent the *NuSTAR* spectrum. Cross markers indicate the multiplicative scaling factors applied to the spectra for visual clarity. Panels (b) and (c) show residuals of the joint fits for NuObs1+*IXPE* and NuObs2+*IXPE*, respectively.

3.3. Phase-resolved polarimetric analysis

We performed a pulse phase-resolved polarimetric analysis by dividing the *IXPE* 2–8 keV data into eight equal phase bins using the ephemeris T_0 = MJD(TDB) 60963.927 and $P_{\rm spin}$ = 5.49 ± 0.05 h (derived from the *IXPE* light curve; see Sect. 3.1). For the spectral-polarimetric analysis in each phase bin, we adopted the XSPEC model `const×tbabs×(po×polconst)`, due to the narrow energy range of *IXPE*. For each phase interval, we calculated PA and PD using XSPEC and `ixpepolarization` (see Sect. 3.2). Table 2 and Fig. 3 summarize the phase-resolved polarization results in the 2–8 keV band. We derived the data points for the normalized Stokes parameters q and u (Figs. 3b and 3c) solely from the model-independent `ixpepolarization` method.

The spectro-polarimetric analysis shows that the phase interval ϕ = 0.250–0.375 (bin 02) shows a PD exceeding its MDP$_{99}$ threshold. In this interval, the PD reaches $10.2^{+3.1}_{-3.0}$% at PA = 83° ± 9° (3.3σ), which corresponds to the pulse-maximum. The phase dependence of the PA suggests a smooth rotation across the pulse by ≈ 150°, from a minimum of about −64° (bin 06) to a maximum of about 87° (bin 00; see also Fig. 5)

Table 1: Best-fitting joint phase-averaged spectral and polarization parameters.

Parameter	Value	
	NuObs1 + *IXPE*	NuObs2 + *IXPE*
$N_{\rm H}$ (10^{22} cm^{-2})	4.3 ± 0.4	5.2 ± 0.4
Γ	0.7 ± 0.1	0.9 ± 0.1
$E_{\rm fold}$ (keV)	12.9 ± 0.6	$14.1^{+0.9}_{-0.8}$
$T_{\rm bbodyrad}$, keV	1.54 ± 0.03	1.41 ± 0.03
$R_{\rm bbodyrad}$, m	590 ± 50	620 ± 50
$E_{\rm Fe\,K\alpha}$ (keV)	6.4 (frozen)	6.4 (frozen)
$\sigma_{\rm Fe\,K\alpha}$ (keV)	0.30 ± 0.08	0.1 (frozen)
$\rm EW_{Fe\,K\alpha}$ (keV)	0.09 ± 0.01	0.05 ± 0.01
$\rm Flux_{2-8}$	4.1 ± 0.1	3.3 ± 0.1
$\rm Luminosity_{2-8}$	7.4 ± 0.1	5.9 ± 0.1
$\rm Flux_{3-79}$	11.8 ± 0.1	8.4 ± 0.1
$\rm Luminosity_{3-79}$	$21.5^{+0.2}_{-0.1}$	15.4 ± 0.1
PD (%)	< 5.4 (MDP$_{99}$)	< 5.1 (MDP$_{99}$)
PA (deg)	88 ± 19	84 ± 22
χ^2/d.o.f.	796/748	586/639

Notes. Fluxes are given in units of 10^{-10} erg s^{-1} cm^{-2}, luminosities in units of 10^{35} erg s^{-1}.

Following the *IXPE* statistical recommendations,[3] we accounted for the use of multiple phase bins and combined the phase-resolved polarization measurements through $\chi^2 = \sum_{j=1}^{J} \left(\Pi_j/\sigma_j\right)^2$, with $2J$ = 16 degrees of freedom (their Eq. 8), to evaluate the overall detection significance across the entire dataset. This yields a global probability for the null hypothesis of $p_{\rm glob} \simeq 4 \times 10^{-4}$, corresponding to a significant detection at 3.3σ (following the convention outlined in Sect. 3.4 of the recommendations).

4. Pulsar geometry

To date, X-ray polarimetry with *IXPE* has been reported for a broad range of accreting pulsars, including disk-fed systems such as Her X-1 (Doroshenko et al. 2022) and 4U 1626−67 (Marshall et al. 2022); wind-fed HMXBs with OB supergiant donors, including Cen X-3 (Tsygankov et al. 2022), Vela X-1 (Forsblom et al. 2023), GX 301−2 (Suleimanov et al. 2023), SMC X-1 (Forsblom et al. 2024), 4U 1538−52 (Loktev et al. 2025), and 4U 1907+09 (Zhou et al. 2025a); as well as Be/X-ray binaries observed during outbursts, such as EXO 2030+375 (Malacaria et al. 2023), GRO J1008−57 (Tsygankov et al. 2023), LS V +44 17 (Doroshenko et al. 2023), Swift J0243.6+6124 (Poutanen et al. 2024a), and 2S 1417−624 (Zhou et al. 2025b).

Typical luminosities during the published *IXPE* observations are of the order $\gtrsim 10^{36}$ erg s^{-1} in OB-supergiant HMXBs and during Be outbursts, although lower values are occasionally reached in persistent low-$\dot{M}$ sources such as X Persei (Mushtukov et al. 2023). The observed polarization is modest, usually a few percent when averaged over the pulse, with phase-dependent enhancements and energy-dependent swings of the PA (Poutanen et al. 2024b). The detection of X-ray polarization from 4U 1954+319 (see Sect. 3.3) marks the first such measurement for an RSG-accreting XRP.

[3] `https://heasarc.gsfc.nasa.gov/docs/ixpe/analysis/IXPE_Stats-Advice.pdf`

Table 2: Phase-resolved polarization and spectral parameters of 4U 1954+319 in the 2–8 keV band, based on model-independent `ixpepolarization` and spectro-polarimetric XSPEC analyses.

Bin	Phase range	$N_{\rm H}$ (10^{22} cm^{-2})	Γ	$\mathrm{PD_{ixpepol}}$ (%)	$\mathrm{PA_{ixpepol}}$ (deg)	$\mathrm{PD_{xspec}}$ (%)	$\mathrm{PA_{xspec}}$ (deg)	$\mathrm{Significance_{xspec}}$ (σ)
00	0.000–0.125	7.5 ± 0.7	1.2 ± 0.1	6.2 ± 3.0	82 ± 14	$6.0^{+3.0}_{-2.9}$	87 ± 15	2.0
01	0.125–0.250	4.8 ± 0.7	0.8 ± 0.1	8.9 ± 3.4	16 ± 11	8.1 ± 3.4	18 ± 12	2.4
02	0.250–0.375	8.0 ± 0.7	1.5 ± 0.1	10.0 ± 3.1	79 ± 9	$10.2^{+3.1}_{-3.0}$	83 ± 9	3.3
03	0.375–0.500	6.1 ± 0.8	1.1 ± 0.1	9.2 ± 3.7	37 ± 11	10.6 ± 3.6	40 ± 10	2.9
04	0.500–0.625	6.1 ± 0.9	1.3 ± 0.2	6.8 ± 4.2	-28 ± 18	5.8 ± 4.1	-21 ± 22	1.4
05	0.625–0.750	6.4 ± 0.9	1.8 ± 0.2	5.8 ± 4.1	-60 ± 20	4.6 ± 4.0	-46 ± 30	1.1
06	0.750–0.875	6.8 ± 0.9	1.8 ± 0.2	9.6 ± 4.1	-62 ± 12	10.5 ± 4.0	-64 ± 11	2.6
07	0.875–1.000	5.8 ± 0.8	1.1 ± 0.1	2.9 ± 3.9	-24 ± 38	4.1 ± 3.8	-7^{+33}_{-27}	1.1

To constrain the geometry of 4U 1954+319, we fit the observed phase dependence of the PA using the rotating vector model (RVM; Radhakrishnan & Cooke 1969; Meszaros et al. 1988; Poutanen 2020), as commonly applied in recent *IXPE* studies of XRPs. In this model, the PA depends on the orientation of the magnetic and spin axes as

$$\tan(\mathrm{PA} - \chi_{\rm p}) = \frac{-\sin\theta\,\sin(\phi - \phi_0)}{\sin i_{\rm p}\cos\theta - \cos i_{\rm p}\sin\theta\cos(\phi - \phi_0)}, \quad (1)$$

where θ is the magnetic obliquity, $i_{\rm p}$ the inclination of the spin axis to the line of sight, $\chi_{\rm p}$ its position angle in the sky (assuming that the radiation is dominated by an ordinary mode) and ϕ_0 is the reference phase.

The application of the RVM implicitly assumes that the observed polarization is dominated by a single polarization mode (ordinary or extraordinary), such that the PA traces the projection of the magnetic axis on the sky. In the case of dominance of the extraordinary mode, the inferred position angle of the pulsar spin axis is $\chi_{\rm p} \pm 90°$. In addition, the presence of an unpulsed phase-independent polarized component would introduce a constant offset in Stokes (q, u) and could bias the inferred PA swing and geometry; this effect is argued to be important in XRPs LS V +44 17 / RX J0440.9+4431 (Doroshenko et al. 2023) and Swift J0243.6+6124 (Poutanen et al. 2024a). For 4U 1954+319, the current data do not require such a component, but its presence cannot be excluded without additional observations.

We performed the RVM fitting using all phase bins. For each bin, we evaluated the likelihood using the analytic probability density function of the measured PA derived by Naghizadeh-Khouei & Clarke (1993):

$$G(\psi) = \frac{1}{\sqrt{\pi}}\left\{\frac{1}{\sqrt{\pi}} + \eta\, \mathrm{e}^{\eta^2}[1 + \mathrm{erf}(\eta)]\right\}\mathrm{e}^{-p_0^2/2}, \quad (2)$$

where $\eta = p_0\cos[2(\psi - \psi_0)]/\sqrt{2}$, ψ is the model PA, ψ_0 the observed PA, and $p_0 = \mathrm{PD}/\sigma_P$ is the polarization signal-to-noise ratio. This approach allowed us to include even low-significance data points.

We explored the parameter space with the Monte Carlo affine-invariant Markov chain (MCMC) sampler EMCEE (Foreman-Mackey et al. 2013), assuming an isotropic prior for the spin axis inclination $p(i_{\rm p}) \propto \sin i_{\rm p}$ and uniform priors for the other parameters. The RVM fit yields two viable geometric solutions given in Table 3 (see the posterior distributions of the parameters in Fig. 6 and the corresponding PA variations in Fig. 3e). To separate the distinct clusters of the posterior, we applied a two-component k-means clustering in the $(\chi_{\rm p}, \phi_0)$ parameter space, which isolates two clusters of the distribution.

Table 3: Parameters of the RVM geometric solutions for binned and unbinned analyses.

Parameter	Binned		Unbinned
	Solution 1	Solution 2	
$i_{\rm p}$ (deg)	101^{+11}_{-8}	145^{+13}_{-14}	144^{+14}_{-15}
θ (deg)	68^{+5}_{-7}	47^{+15}_{-17}	49^{+16}_{-18}
$\chi_{\rm p}$ (deg)	16 ± 8	139^{+13}_{-12}	138^{+10}_{-12}
ϕ_0	$0.47^{+0.03}_{-0.02}$	0.75 ± 0.03	0.76 ± 0.02

Notes. Position angle $\chi_{\rm p} = 139°$ is equivalent to $-41°$ under the 180° modulo; other equivalent representations follow the same periodicity.

This behavior is expected given the limited polarization significance in several phase bins. In the corner plot, the two clusters exhibit peaks of different heights. Model comparison using the Akaike Information Criterion (AIC; Akaike 1974), computed as $\mathrm{AIC} = 2k - 2\ln L$ (with the same number of parameters k for both solutions), yields $\Delta\mathrm{AIC} \approx 3.5$, indicating only a marginal preference for Solution 2 and leaving the degeneracy unresolved.

We performed complementary RVM analysis directly in the Stokes (q, u) domain. For each phase bin i, the model predicts

$$q_i^{\rm mod} = P_{0,i}\cos(2\psi_i), \qquad u_i^{\rm mod} = P_{0,i}\sin(2\psi_i), \quad (3)$$

where ψ_i is the RVM PA and $P_{0,i}$ is the PD, treated as an independent free parameter for each bin. Assuming Gaussian uncertainties in the measured Stokes parameters $(q_i^{\rm obs}, u_i^{\rm obs})$ with standard deviations σ_i, the likelihood takes the form

$$\ln\mathcal{L} = -\frac{1}{2}\chi^2 + \mathrm{const}, \quad (4)$$

where

$$\chi^2 = \sum_i \left[\frac{(q_i^{\rm obs} - q_i^{\rm mod})^2}{\sigma_i^2} + \frac{(u_i^{\rm obs} - u_i^{\rm mod})^2}{\sigma_i^2}\right]. \quad (5)$$

The posterior samples separate into two distinct geometric clusters in parameter space, which does not show a preferred configuration. The RVM provides an adequate description of the phase-resolved polarization data, with a reduced $\chi^2 \simeq 1.7$.

We performed an unbinned, event-by-event RVM fit (Fig. 7) using measured normalized Stokes parameters (q_k, u_k) for each photon together with the per-event modulation factor $\mu(E)$ (González-Caniulef et al. 2023). In this case, the likelihood is written as a product of per-photon probabilities of the form $f_k = (2\pi)^{-1}[1 + \mu_k P_0(q_k^\gamma q_k^{\rm m} + u_k^\gamma u_k^{\rm m})]$, where (q_k^γ, u_k^γ) are the measured Stokes parameters of photon k, $(q_k^{\rm m}, u_k^{\rm m})$ are the model predictions for its rotational phase, and P_0 is treated as a free parameter.

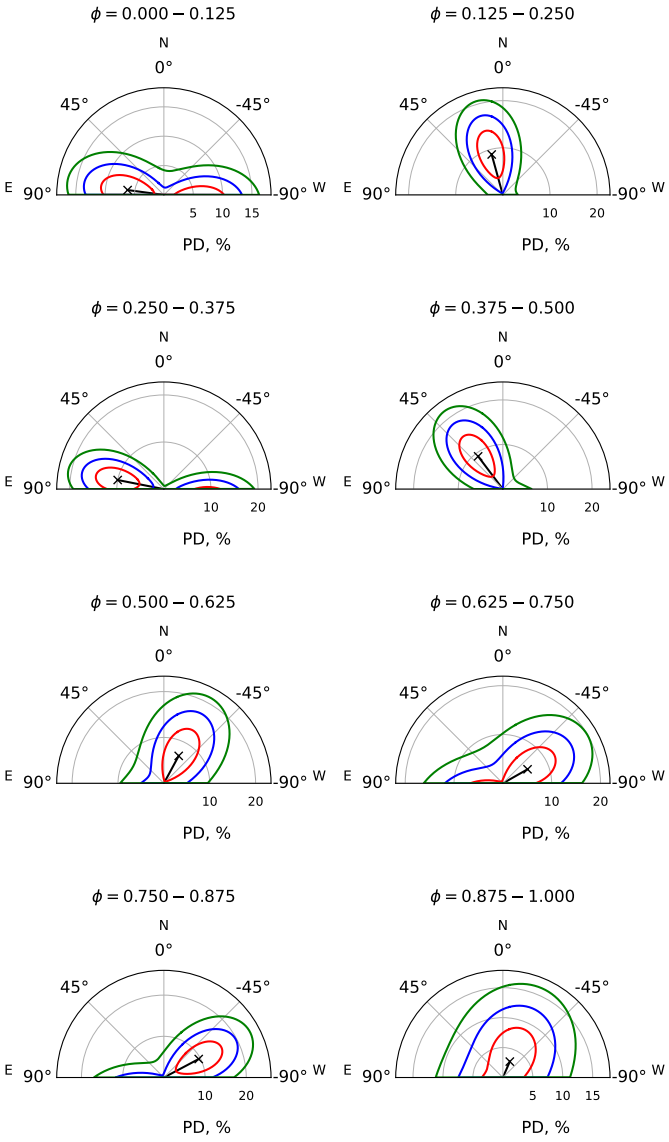

Fig. 5: Protractor plots showing phase-resolved PD (radius) and PA (azimuth) in the 2–8 keV range. Contours indicate 1, 2, and 3σ CLs for two parameters, shown in red, blue, and green, respectively. The cross marks the best-fit point, and the line indicates the polarization direction.

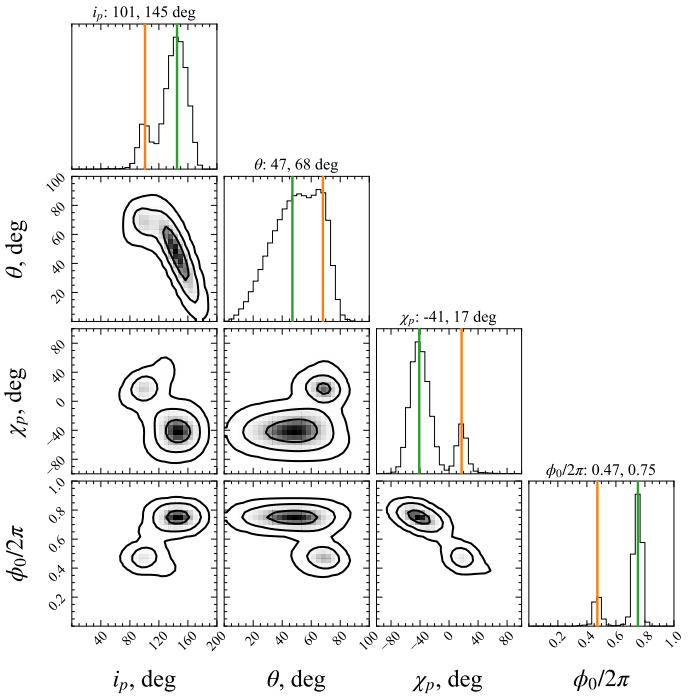

Fig. 6: Posterior distributions of the RVM parameters derived from the phase-resolved PAs (spectro-polarimetric analysis). Contours correspond to 1σ, 2σ, and 3σ CLs. The histograms show the normalized one-dimensional distributions for a given parameter derived from the posterior samples. Vertical lines in the diagonal panels mark the median values of the two posterior clusters.

The *IXPE* Level-2 event lists provide Stokes-like columns Q_k and U_k, defined as $Q_k = 2\cos(2\psi_k)$ and $U_k = 2\sin(2\psi_k)$ (see Sect. 4.1 of the *IXPE* Quick Start Guide[4]), whereas the González-Caniulef et al. (2023) likelihood is formulated in terms of normalized quantities $q_k^\gamma = \cos(2\psi_k)$ and $u_k^\gamma = \sin(2\psi_k)$. We therefore used $q_k^\gamma = Q_k/2$ and $u_k^\gamma = U_k/2$ in the unbinned likelihood.

The unbinned posterior contains two previously considered solutions, but they are now highly asymmetric in statistical weight. Information-criterion comparison shows that Solution 2 is strongly favored (ΔAIC $\approx$ 13), allowing us to unambiguously identify it as the statistically preferred geometry. The geometric parameters of the preferred solution remain consistent with the binned results within their respective uncertainties (see Table 3), and the phase-independent polarization is characterized by PD = 6.1 ± 1.1%. This unbinned estimation of the PD explicitly accounts for the phase-dependent PA rotation, avoids cancellation of the Stokes vectors over the pulse, and yields a significant detection, unlike the phase-averaged analysis.

Thus, polarimetric analysis yields magnetic obliquity in the range $\theta \simeq 30°$–$65°$, corresponding to an intermediate viewing geometry. In this configuration, the angle between the line of sight and the magnetic axis varies significantly over the spin period, which does not favor simple or symmetric pulse profiles. The complexity of the flux profile is also driven by the properties of the emitting regions and the accretion process, including inhomogeneities such as clumpy stellar-wind accretion previously suggested for this source (Bozzo et al. 2022).

Such an intermediate obliquity is consistent with the range of values inferred for other accreting XRPs observed with *IXPE* (see, for a recent review, Poutanen et al. 2024b), which span from nearly aligned to nearly orthogonal rotators. At the same time, 4U 1954+319 complements the existing *IXPE* sample by providing the first geometric constraints for an extremely slowly rotating XRP accreting from the wind of a red supergiant companion.

5. Conclusions

In this work, we present the first X-ray polarimetric study of the red supergiant XRP 4U 1954+319 with *IXPE*. Our main results can be summarized as follows.

1. The *IXPE* observation confirms the presence of very slow coherent pulsations with a spin period of $P_{\rm spin} = 5.49 \pm 0.05$ h.

[4] https://heasarc.gsfc.nasa.gov/docs/ixpe/analysis/ixpe_quickstart.pdf

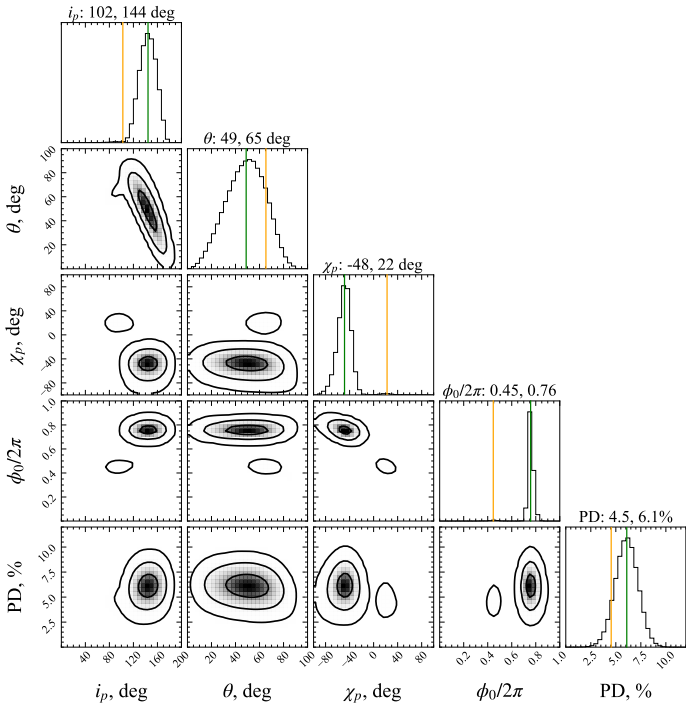

Fig. 7: Posterior distributions of the RVM parameters from the unbinned analysis. Contours correspond to 1σ, 2σ, and 3σ CLs. The histograms show the normalized one-dimensional distributions for a given parameter derived from the posterior samples. Vertical lines in the diagonal panels mark the median values of the two posterior clusters.

The 2–8 keV pulse profile has two maxima with multiple subpeaks and exhibits a PF of 55 ± 1%.

2. No significant phase-averaged polarization is detected in the 2–8 keV band, with an MDP_{99} of 4.9%.
3. The phase-resolved analysis identifies one phase bin in which the PD exceeds its MDP_{99}. At pulse maximum, the measurement yields PD = $10.2^{+3.1}_{-3.0}$% and PA = 83° ± 9°. Together with lower-significance measurements in the remaining bins, these results trace a smooth rotation of the PA across the pulse by ≈ 150°. When all phase bins are combined in a joint statistical test, the overall detection significance reaches 3.3σ.
4. Fitting the phase dependence of the binned polarimetric data with the RVM yields two plausible geometric solutions. The unbinned analysis indicates that one of them statistically dominates, and we therefore adopt it as the preferred geometry, yielding a phase-independent PD of 6.1 ± 1.1% in the 2–8 keV band.

Acknowledgements. This work reports observations obtained with the Imaging X-ray Polarimetry Explorer (IXPE), a joint US (NASA) and Italian (ASI) mission, led by Marshall Space Flight Center (MSFC). The research uses data products provided by the IXPE Science Operations Center (MSFC), using algorithms developed by the IXPE Collaboration (MSFC, Istituto Nazionale di Astrofisica - INAF, Istituto Nazionale di Fisica Nucleare - INFN, ASI Space Science Data Center - SSDC), and distributed by the High-Energy Astrophysics Science Archive Research Center (HEASARC). This research also has made use of the *NuSTAR* Data Analysis Software (NUSTARDAS) jointly developed by the ASI Science Data Centre (ASDC, Italy) and Caltech. We are grateful to the *IXPE* and *NuSTAR* teams for the approval and rapid scheduling of the observations. AS acknowledges support from the Jenny and Antti Wihuri Foundation (grant no. 00240331). This research was supported by the International Space Science Institute (ISSI) in Bern, through International Team project 25-657 'Polarimetric Insights into Extreme Magnetism' and the Research Council of Finland Centre of Excellence in Neutron-Star Physics (grant 374064). We thank the anonymous referee for their careful reading of the paper and thoughtful suggestions, which helped improve the clarity of the results.

References

Akaike, H. 1974, IEEE Transactions on Automatic Control, 19, 716
Arnaud, K. A. 1996, in ASP Conf. Ser., Vol. 101, Astronomical Data Analysis Software and Systems V, ed. G. H. Jacoby & J. Barnes (San Francisco: Astron. Soc. Pac.), 17–20
Avakyan, A., Neumann, M., Zainab, A., et al. 2023, A&A, 675, A199
Bahramian, A. & Degenaar, N. 2024, in Handbook of X-ray and Gamma-ray Astrophysics, ed. C. Bambi & A. Santangelo (Singapore: Springer), 3657–3718
Baldini, L., Barbanera, M., Bellazzini, R., et al. 2021, Astroparticle Physics, 133, 102628
Bozzo, E., Ferrigno, C., Oskinova, L., & Ducci, L. 2022, MNRAS, 510, 4645
Corbet, R., Barbier, L., Barthelmy, S., et al. 2006, The Astronomer's Telegram, 797, 1
Corbet, R. H. D., Sokoloski, J. L., Mukai, K., Markwardt, C. B., & Tueller, J. 2008, ApJ, 675, 1424
De, K., Daly, F. A., & Soria, R. 2024, MNRAS, 528, L38
Doroshenko, V., Poutanen, J., Heyl, J., et al. 2023, A&A, 677, A57
Doroshenko, V., Poutanen, J., Tsygankov, S. S., et al. 2022, Nature Astronomy, 6, 1433
Enoto, T., Sasano, M., Yamada, S., et al. 2014, ApJ, 786, 127
Foreman-Mackey, D., Hogg, D. W., Lang, D., & Goodman, J. 2013, PASP, 125, 306
Forsblom, S. V., Poutanen, J., Tsygankov, S. S., et al. 2023, ApJ, 947, L20
Forsblom, S. V., Tsygankov, S. S., Poutanen, J., et al. 2024, A&A, 691, A216
Ghosh, P. & Lamb, F. K. 1979, ApJ, 234, 296
González-Caniulef, D., Caiazzo, I., & Heyl, J. 2023, MNRAS, 519, 5902
Harrison, F. A., Craig, W. W., Christensen, F. E., et al. 2013, ApJ, 770, 103
Hinkle, K. H., Lebzelter, T., Fekel, F. C., et al. 2020, ApJ, 904, 143
Kislat, F., Clark, B., Beilicke, M., & Krawczynski, H. 2015, Astroparticle Physics, 68, 45
Loktev, V., Forsblom, S. V., Tsygankov, S. S., et al. 2025, A&A, 698, A22
Malacaria, C., Heyl, J., Doroshenko, V., et al. 2023, A&A, 675, A29
Mao, Y.-H. & Li, X.-D. 2024, MNRAS, 533, 386
Marcu, D. M., Fürst, F., Pottschmidt, K., et al. 2011, ApJ, 742, L11
Marshall, H. L., Ng, M., Rogantini, D., et al. 2022, ApJ, 940, 70
Masetti, N., Orlandini, M., Palazzi, E., Amati, L., & Frontera, F. 2006, A&A, 453, 295
Meszaros, P., Novick, R., Szentgyorgyi, A., Chanan, G. A., & Weisskopf, M. C. 1988, ApJ, 324, 1056
Mushtukov, A. & Tsygankov, S. 2024, in Handbook of X-ray and Gamma-ray Astrophysics, ed. C. Bambi & A. Santangelo (Singapore: Springer), 4105–4176
Mushtukov, A. A., Tsygankov, S. S., Poutanen, J., et al. 2023, MNRAS, 524, 2004
Naghizadeh-Khouei, J. & Clarke, D. 1993, A&A, 274, 968
Neumann, M., Avakyan, A., Doroshenko, V., & Santangelo, A. 2023, A&A, 677, A134
Poutanen, J. 2020, A&A, 641, A166
Poutanen, J., Tsygankov, S. S., Doroshenko, V., et al. 2024a, A&A, 691, A123
Poutanen, J., Tsygankov, S. S., & Forsblom, S. V. 2024b, Galaxies, 12, 46
Radhakrishnan, V. & Cooke, D. J. 1969, Astrophys. Lett., 3, 225
Salganik, A., Kong, L., Forsblom, S. V., et al. 2025, The Astronomer's Telegram, 17464, 1
Shakura, N., Postnov, K., Kochetkova, A., & Hjalmarsdotter, L. 2012, MNRAS, 420, 216
Soffitta, P., Baldini, L., Bellazzini, R., et al. 2021, AJ, 162, 208
Suleimanov, V. F., Forsblom, S. V., Tsygankov, S. S., et al. 2023, A&A, 678, A119
Tsygankov, S. S., Doroshenko, V., Mushtukov, A. A., et al. 2023, A&A, 675, A48
Tsygankov, S. S., Doroshenko, V., Poutanen, J., et al. 2022, ApJ, 941, L14
Wang, X. I. & Li, X.-D. 2025, ApJ, 985, 12
Weisskopf, M. C., Soffitta, P., Baldini, L., et al. 2022, JATIS, 8, 026002
Wilms, J., Allen, A., & McCray, R. 2000, ApJ, 542, 914
Zhou, M., Ducci, L., Liu, H., et al. 2025a, A&A, 700, A283
Zhou, M., Wang, P., Liu, H., et al. 2025b, arXiv e-prints, arXiv:2508.16417